

# Coulomb Drag of Massless Fermions in Graphene

S. Kim,<sup>1</sup> I. Jo,<sup>2</sup> J. Nah,<sup>1</sup> Z. Yao,<sup>2</sup> S. K. Banerjee,<sup>1</sup> and E. Tutuc<sup>1</sup>

<sup>1</sup>*Microelectronics Research Center, The University of Texas at Austin, Austin, TX 78758*

<sup>2</sup>*Department of Physics, The University of Texas at Austin, Austin, TX 78712*

(Dated: November 4, 2018)

Using a novel structure, consisting of two, independently contacted graphene single layers separated by an ultra-thin dielectric, we experimentally measure the Coulomb drag of massless fermions in graphene. At temperatures higher than 50 K, the Coulomb drag follows a temperature and carrier density dependence consistent with the Fermi liquid regime. As the temperature is reduced, the Coulomb drag exhibits giant fluctuations with an increasing amplitude, thanks to the interplay between coherent transport in the graphene layer and interaction between the two layers.

PACS numbers: 73.43.-f, 71.35.-y, 73.22.Gk

Two layers of carriers in close proximity can, in certain conditions favor correlated electron states with no counterpart in the single layer physics. The most notable is the formation of pairs of electrons and holes residing in opposing layers (indirect excitons), which can flow with no dissipation [1]. Such phenomena have been observed in electron-electron or hole-hole double quantum wells in high magnetic fields, when the lowest Landau level in each layer is half-full, and pairs of carriers and vacancies residing in opposite layers form as a result of inter-layer interaction [2], as well as in trapped microcavity polaritons [3]. Graphene, a monolayer of carbon atoms in a honeycomb lattice [4, 5], offers a unique system to investigate electron physics in interacting bilayers. The zero energy band-gap in graphene allows a seamless transition between electrons and holes in each layer, and obviates the large inter-layer electric field required to simultaneously induce electrons and holes in GaAs/AlGaAs bilayers [6]. Moreover, theoretical arguments suggest that a closely spaced electron-hole graphene bilayer favors dipolar superfluidity at elevated temperatures [7]. Here we demonstrate independently contacted graphene bilayers, and investigate the Coulomb drag in this system.

Two main ingredients render the realization of independently contacted graphene bilayers challenging. First, an ultra-thin yet highly insulating dielectric is required to separate the two layers. Second, a graphene transfer process with minimum or no degradation is needed to create the second layer of the structure investigated here. The fabrication of our independently contacted graphene bilayers, consisting of two graphene monolayers separated by a dielectric is described in Fig. 1. First, the bottom graphene layer is mechanically exfoliated onto a 280nm thick SiO<sub>2</sub> dielectric, thermally grown on a highly doped Si substrate. Standard e-beam lithography, metal lift-off, and etching are used to define a Hall bar on the bottom layer [Fig. 1(a)]. A 7 nm thick Al<sub>2</sub>O<sub>3</sub> is then deposited on the bottom layer using a 2 nm oxidized Al interfacial layer, followed by 5 nm of Al<sub>2</sub>O<sub>3</sub> atomic layer deposition [8]. The second, top graphene layer is also mechanically exfoliated on a similar SiO<sub>2</sub>/Si substrate.

A poly methyl metacrylate (PMMA) film is then applied on the top layer and cured. Using an NaOH etch [9], the PMMA film along with the graphene layer and the alignment marks are detached from the host substrate, forming a free standing membrane. The membrane is placed face down on the substrate containing the bottom graphene layer [Fig. 1(b)], and aligned with it. A Hall bar device geometry is subsequently defined on the top layer [Fig. 1(c)]. Ten back-gated, independently contacted graphene bilayers have been fabricated and investigated in this study, all with similar results. We focus here on data collected from three samples, labeled 1, 2, and 3, with mobilities between 4,200-12,000 cm<sup>2</sup>/Vs for the bottom layer, 4,500-22,000 cm<sup>2</sup>/Vs for the top layer, and with inter-layer resistances of 1-20 GΩ. We note that these structures are markedly different from graphene bilayers exfoliated from natural graphite, consisting of two graphene monolayers in Bernal stacking [10].

We now turn to the individual layer characterization in independently contacted graphene bilayers. The layer resistivities ( $\rho$ ) and Hall densities measured for sample 1 at a temperature  $T=4.2$  K, as a function of back-gate bias ( $V_{BG}$ ) are shown in Fig. 2(a) and 2(b), respectively. The bottom layer dependence on the applied  $V_{BG}$  shows ambipolar conduction and a finite resistance at the charge neutrality (Dirac) point, consistent with the expected response of gated monolayer graphene where disorder generates electron-hole puddles at the Dirac point [11]. More interestingly, the top layer resistivity also changes as a result of the applied  $V_{BG}$ . This observation indicates an incomplete screening of the gate-induced electric field by the bottom layer, which is most pronounced in the vicinity of the charge neutrality point, a direct consequence of the reduced density of states in graphene. As we show below, we can quantitatively explain the layer resistivities and carrier densities dependence on  $V_{BG}$ .

Figure 2(c) shows the band diagram of the graphene bilayer at  $V_{BG}=0$  V; for simplicity the gate Fermi energy and the charge neutrality point in the two layers are assumed to be at the same energy. Once a finite  $V_{BG}$  is applied, finite charge densities are induced in both

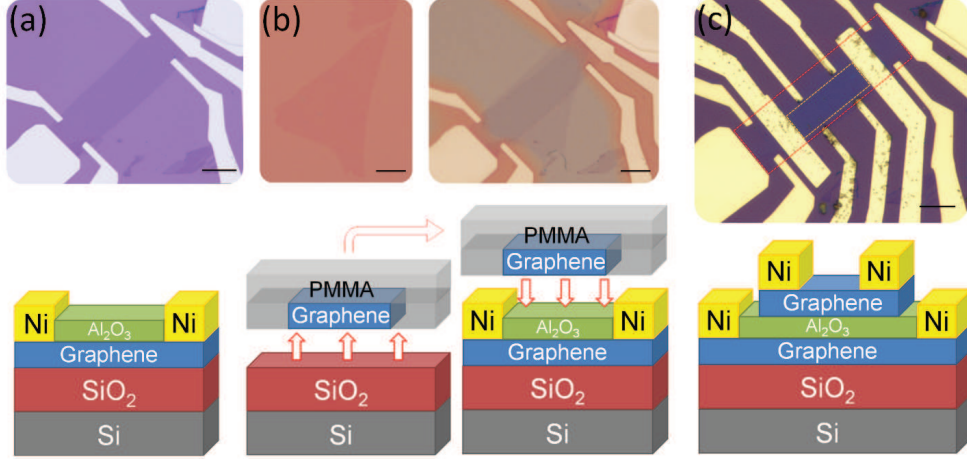


FIG. 1: (color online) Optical micrographs (top) and schematic representation (bottom) outlining the fabrication process of an independently contacted graphene bilayer. (a) Hall bar device fabrication on the bottom graphene layer, followed by the  $\text{Al}_2\text{O}_3$  inter-layer dielectric deposition. (c) Top graphene layer isolation on a separate substrate, followed by transfer onto the bottom layer using a PMMA membrane spin-on and NaOH etching. (c) Top graphene layer Hall bar realization, using graphene etching, lithography, metal deposition, and lift-off. The yellow and red dashed contours in the optical micrograph represent the top and bottom layers, respectively. The scale bar in all panels is  $10\ \mu\text{m}$ .

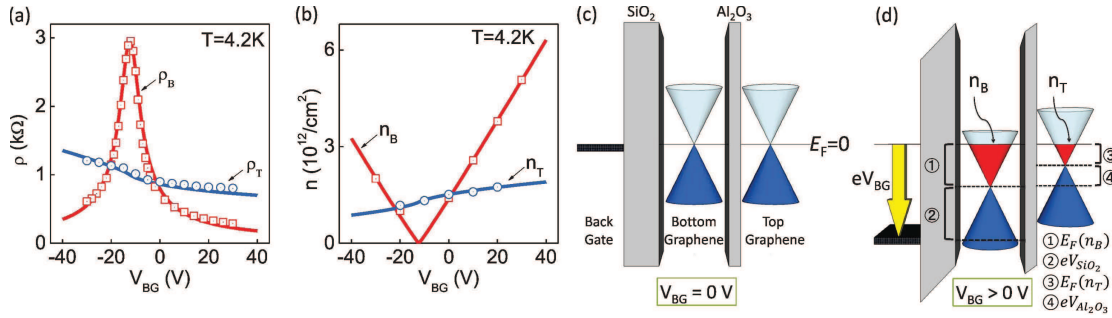


FIG. 2: (color online) (a) Top and bottom layer four-point resistivity vs.  $V_{BG}$ , measured at  $T=4.2\ \text{K}$  in sample 1. (b) Layer densities vs.  $V_{BG}$  at  $T=4.2\ \text{K}$ . Depending on the applied  $V_{BG}$ , both electrons and holes can be induced in the bottom layer; the top layer contains electrons in the available  $V_{BG}$  window, owing in part to unintentional  $n$ -type doping. The symbols in panels (a) and (b) represent experimental data, while solid lines represent the calculated  $V_{BG}$  dependences according to Eqs. (1) and (2). (c) Schematic representation of the band diagrams across the graphene bilayer heterostructure at  $V_{BG}=0\ \text{V}$ . For simplicity both layers are assumed to be at the charge neutrality point, and aligned with the back-gate Fermi level. The layer thickness is exaggerated to show the energy wave-vector Dirac cones. (d) Band diagram in the same heterostructure under an applied positive  $V_{BG}$ . The two layers are assumed to be grounded, hence their respective Fermi levels remain at  $0\ \text{V}$ . In addition to the voltage drop ( $V_{\text{SiO}_2}$ ) across the  $\text{SiO}_2$  bottom dielectric, an electric field is created across the inter-layer  $\text{Al}_2\text{O}_3$  dielectric, resulting in finite electron densities being induced in both layers;  $V_{\text{Al}_2\text{O}_3}$  is the voltage drop across the  $\text{Al}_2\text{O}_3$  layer.

top ( $n_T$ ) and bottom ( $n_B$ ) layers [Fig. 2(d)]. The difference between the gate and bottom layer Fermi levels is distributed partly across the  $\text{SiO}_2$  dielectric, and partly on the Fermi energy of the bottom graphene layer:  $eV_{BG} = e^2(n_B + n_T)/C_{\text{SiO}_2} + E_F(n_B)$  (1);  $E_F(n) = \hbar v_F \sqrt{\pi n}$  is the graphene Fermi energy measured with respect to the charge neutrality point at a carrier density  $n$ ,  $e$  represents the electron charge,  $v_F = 1.1 \times 10^6\ \text{m/s}$  is the graphene Fermi velocity, and  $C_{\text{SiO}_2}$  denotes the  $\text{SiO}_2$  dielectric capacitance per unit area. Similarly, the Fermi energy difference between the two layers is responsible for the potential drop across the  $\text{Al}_2\text{O}_3$  inter-layer di-

electric:  $E_F(n_B) = e^2 n_T / C_{\text{Al}_2\text{O}_3} + E_F(n_T)$  (2);  $C_{\text{Al}_2\text{O}_3}$  is the  $\text{Al}_2\text{O}_3$  dielectric capacitance per unit area. The finite Fermi energy of the bottom layer,  $E_F(n_B)$  in Eq. (2), plays the same role with respect to the top layer, as the applied  $V_{BG}$  in Eq. (1) for the bottom layer. Equations (1) and (2) allow us to determine  $n_B$  and  $n_T$  as a function of  $V_{BG}$ . This model can be adjusted to include finite layer densities at  $V_{BG}=0\ \text{V}$ . The layer resistivity dependence on  $V_{BG}$  can be understood using a Drude model  $\rho_{T,B} = (n_{T,B}^* e \mu_{T,B})^{-1}$ , where  $\mu_T$ , and  $\mu_B$  are the top and bottom layer mobilities, and the layer densities are adjusted to allow for finite carrier densities

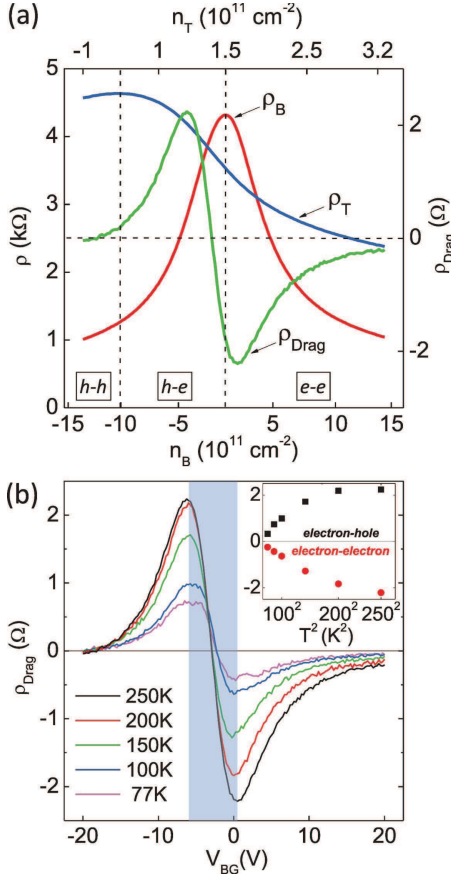


FIG. 3: (color online) Coulomb drag in graphene bilayers. (a) Layer resistivity ( $\rho$ ) and  $\rho_{\text{Drag}}$  vs. layer densities for sample 2, measured by sweeping  $V_{\text{BG}}$  at  $T=250$  K. The charge neutrality points of both layers are captured in the experimentally accessible  $V_{\text{BG}}$  window, allowing the bilayer to probe three different regimes: hole-hole, electron-hole, and electron-electron. (b)  $\rho_{\text{Drag}}$  vs.  $V_{\text{BG}}$  measured at different  $T$  values, from 250 K to 77 K (solid lines). Inset: maximum  $\rho_{\text{Drag}}$  measured in the electron-hole and electron-electron regimes vs.  $T^2$ . The  $V_{\text{BG}}$  axis of panel (b) applies to both panels.

( $n_{0T}$ ,  $n_{0B}$ ) at the charge neutrality point. The data of Figs. 2(a) and 2(b) show a good agreement between the measured layer resistivities and densities (symbols), and the calculations (solid lines). The layer mobilities, determined from Hall measurements, are  $\mu_B=5,400 \text{ cm}^2/\text{Vs}$ , and  $\mu_T=4,500 \text{ cm}^2/\text{Vs}$  at  $T=4.2\text{K}$ .

Key insight into the physics of the graphene bilayer system, as well as the ground state of mono-layer graphene can be gained from a Coulomb drag measurement [12, 13]. A current ( $I_{\text{Drive}}$ ) flown in one (drive) layer leads to a momentum transfer between the two layers, thanks to the inter-layer electron-electron interaction. To counter this momentum transfer, a longitudinal voltage ( $V_{\text{Drag}}$ ) builds up in the opposite (drag) layer. The polarity of  $V_{\text{Drag}}$  depends on the carrier type in the two layers, and is opposite (same) polarity as the voltage drop in the drive layer when the both layers have the

same (opposite) type of carriers. The drag resistivity is defined as  $\rho_{\text{Drag}} = (W/L)V_{\text{Drag}}/I_{\text{Drive}}$ , where  $L$  and  $W$  are the length and width of the region where drag occurs. An example of measured  $\rho_{\text{Drag}}$  vs.  $V_{\text{BG}}$  at  $T=250$  K in sample 2 is shown in Fig. 3(a), along with the top and bottom layer resistivities,  $\rho_T$  and  $\rho_B$ . Unlike sample 1 data (Fig. 2), the charge neutrality (Dirac) points of both layers can be captured in the experimentally accessible  $V_{\text{BG}}$  window. Consequently, depending on the  $V_{\text{BG}}$  value, sample 2 can probe three different regimes: a *hole-hole* bilayer, for  $V_{\text{BG}} < -15$  V, an *electron-hole* bilayer for  $-15 \text{ V} < V_{\text{BG}} < -2$  V, and an *electron-electron* bilayer for  $V_{\text{BG}} > -2$  V. The dependence of  $\rho_B$  and  $\rho_T$  on  $V_{\text{BG}}$  of Fig. 3 is also in good agreement with the model presented in Fig. 2. Consistent with the above argument,  $\rho_{\text{Drag}}$  is positive in the electron-hole bilayer regime, negative in the hole-hole or electron-electron regime, and changes sign when either the top or the bottom layer are at the charge neutrality point. The standard consistency checks [13] have been performed to ensure the measured drag voltage is not affected by inter-layer leakage current.

For two closely spaced two-dimensional systems, when the ground state of each layer is assumed to be a Fermi liquid, and the inter-layer interaction is treated as a perturbation, the  $\rho_{\text{Drag}}$  depends on layer density ( $n$ ) as  $\propto 1/n^{3/2}$ , on temperature as  $\propto T^2$ , and inter-layer distance ( $d$ ) as  $\propto 1/d^4$  [13]. Likewise, the Coulomb drag resistivity in graphene, calculated in the Fermi liquid regime using Boltzmann transport formalism and the random phase approximation for the interaction dynamic screening is [14]:  $\rho_{\text{Drag}} = -\frac{\hbar}{e^6} \frac{\zeta(3)}{32} \frac{(k_B T)^2}{d^4} \frac{\epsilon^2}{n_B^{3/2} n_T^{3/2}}$  (3);  $k_B$  is the Boltzmann constant,  $\zeta(3) \cong 1.2$ ,  $\epsilon$  is the dielectric permittivity. A separate effect which has been theoretically advanced as the representative Coulomb drag mechanism in graphene is trigonal warping [15]. Figure 3(b) data shows  $\rho_{\text{Drag}}$  vs.  $V_{\text{BG}}$  measured for sample 2 for  $T$  values between 77 K and 250 K. Away from the charge neutrality point of the bottom layer, the  $\rho_{\text{Drag}}$  magnitude increases with reducing  $n_B$  following a  $\propto 1/n_B^{3/2}$  dependence, consistent with the expected behaviour in the Fermi liquid regime [14]. We note however that the magnitude of  $\rho_{\text{Drag}}$  is a factor of  $\sim 10^2$  lower than the values expected according to Eq. (3). The  $\rho_{\text{Drag}} \propto (k_B T)^2$  dependence, which stems from the allowed phase space where electron-electron scattering occurs, is followed closely for temperatures higher than 70 K (Fig. 3(b) inset). Figure 3 data shows a smooth crossover for  $\rho_{\text{Drag}}$  through  $0 \text{ } \Omega$ , from the electron-hole to the electron-electron regime [blue corridor of Fig. 3(b)]. The crossover can be explained by the co-existence of electron and hole puddles near the charge neutrality point of the bottom layer, which generate drag electric fields of opposite sign, and cancel the  $\rho_{\text{Drag}}$ .

A remarkable transition in the drag resistance is observed for  $T$  lower than 50 K (Fig. 4). As  $T$  is reduced, the  $\rho_{\text{Drag}}$  data starts to develop fluctuations superposed

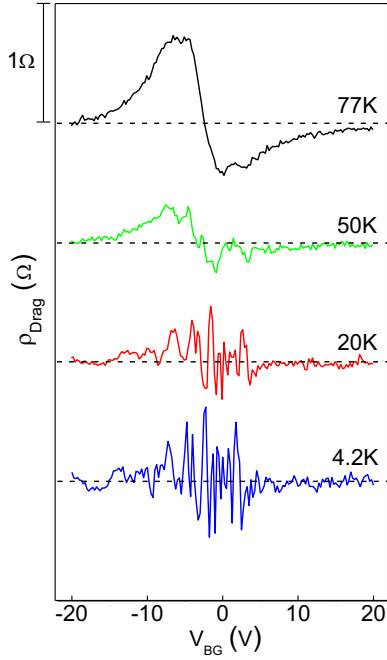


FIG. 4: (color online)  $\rho_{Drag}$  vs.  $V_{BG}$  measured in sample 2 for  $T \leq 77$  K. As  $T$  is reduced,  $\rho_{Drag}$  exhibits mesoscopic fluctuations with increasing amplitude, which fully obscure the average drag at the lowest temperatures. The traces are shifted for clarity; the horizontal dashed lines indicate 0  $\Omega$  for each trace.

on the average  $\rho_{Drag}$  vs.  $V_{BG}$  dependence of Fig. 3 and Eq.(3), valid for diffusive transport. The  $\rho_{Drag}$  fluctuations, which are reproducible in different measurements, grow in amplitude as  $T$  is reduced, and fully obscure the average diffusive drag below 20 K. This manifestation of mesoscopic physics at elevated temperatures is a consequence of the phase coherence length ( $L_\varphi$ ) becoming comparable to the sample dimensions, and represents the counterpart of universal conductance fluctuations [16] in Coulomb drag [17, 18]. Figure 4 data reveal that  $\rho_{Drag}$  fluctuation amplitude reaches a maximum near the charge neutrality point of the bottom layer ( $V_{BG} = -1$  V), and increases, albeit slowly as  $T$  is decreased. Theoretical arguments [18] indicate that the drag conductivity ( $\sigma_{Drag} = \rho_{Drag}/\rho_T\rho_B$ ) fluctuation amplitude ( $\delta\sigma_{Drag}$ ) depends on relevant length scales and temperature as  $\delta\sigma_{Drag} \propto T \cdot (L_\varphi^3 l)/L$ ;  $l$  is the electron mean free path. For the temperature range examined in Fig. 4,  $l$  can be considered constant, as the mobility is weakly dependent on  $T$ . Assuming the electron-electron interaction is the main phase-breaking mechanism in graphene [19], hence  $L_\varphi = l\sqrt{E_F/2k_B T}$ , the  $T$  dependence of  $\delta\sigma_{Drag}$  and  $\delta\rho_{Drag}$  should follow a  $\propto T^{-1/2}$  dependence, in good agreement with Fig. 4 data.

To probe the signature of weak localization in Coulomb drag, in Fig. 5 we show an example of  $\rho_{Drag}$  vs. perpendicular magnetic field ( $B$ ) data, measured in sam-

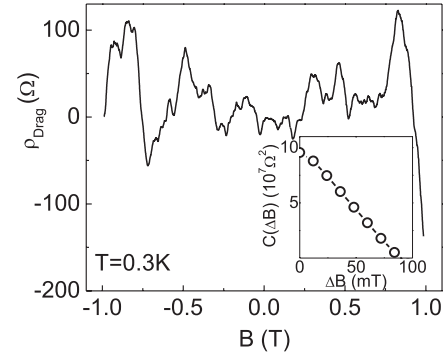


FIG. 5:  $\rho_{Drag}$  vs.  $B$  measured at  $T=0.3$  K in sample 3, showing mesoscopic fluctuations similar to Fig. 4 data. Inset:  $\rho_{Drag}$  vs.  $B$  data autocorrelation.

ple 3 at  $T=0.3$  K and  $V_{BG}=0$  V; both layers contain electrons with layer densities  $n_T = 1.4 \times 10^{11} \text{ cm}^{-2}$ , and  $n_B = 1.5 \times 10^{11} \text{ cm}^{-2}$ . Similar to the  $V_{BG}$  dependence of Fig. 4, the  $\rho_{Drag}$  vs.  $B$  data shows reproducible mesoscopic fluctuations. The auto-correlation function ( $C(\Delta B)$ ) of Fig. 5 data reveals a correlation field  $B_c = 47$  mT, which corresponds to a phase coherence length  $L_\varphi = \sqrt{\hbar/eB_c} = 300$  nm. Similar  $L_\varphi$  values have been extracted from ensemble average measurements using scanning gate microscopy [20].

In summary, we demonstrate independently contacted graphene bilayers, and probe the Coulomb drag in this system. At elevated temperatures the drag resistance dependence on density and temperature are consistent with the Fermi liquid theory. At reduced temperatures, the drag exhibits macroscopic fluctuations with increasing amplitude, which obscure the average drag, a result of the interplay between electron-electron interaction and phase coherent transport.

We thank A. H. MacDonald, W. K. Tse, and B. Narozhny for discussions, and NRI-SWAN for support. Part of our work was performed at the National High Magnetic Field Laboratory, which is supported by NSF (DMR-0654118), the State of Florida, and DOE.

- 
- [1] Y. E. Lozovik, V. I. Yudson, JETP Lett. **22**, 274 (1975).
  - [2] J. P. Eisenstein, A. H. MacDonald, Nature **432**, 691 (2004).
  - [3] R. Balili *et al.*, Science **316**, 1007 (2007).
  - [4] K. S. Novoselov *et al.*, Science **306**, 666 (2004).
  - [5] K. S. Novoselov *et al.*, Nature **438**, 197 (2005); Y. Zhang *et al.*, Nature **438**, 201 (2005).
  - [6] A. F. Croxall *et al.*, Phys. Rev. Lett. **101**, 246801 (2008); J. A. Seamons *et al.*, Phys. Rev. Lett. **102**, 026804 (2009).
  - [7] H. Min *et al.*, Phys. Rev. B **78**, 121401 (2008).
  - [8] S. Kim *et al.*, Appl. Phys. Lett. **94**, 062107 (2009).
  - [9] A. Reina *et al.*, J. Phys. Chem. C **112**, 17741 (2008).

- [10] E. McCann, V. I. Fal'ko, Phys. Rev. Lett. **96**, 086805 (2006).
- [11] S. Adam *et al.*, Proc. Natl. Acad. Sci. U.S.A. **104**, 18392 (2007).
- [12] P. M. Solomon *et al.*, Phys. Rev. Lett. **63**, 2508 (1989).
- [13] T. J. Gramila *et al.*, Phys. Rev. Lett. **66**, 1216 (1991).
- [14] W.-K. Tse *et al.*, Phys. Rev. B **76**, 081401 (2007).
- [15] B. N. Narozhny, Phys. Rev. B **76**, 153409 (2007).
- [16] P. A. Lee, A. D. Stone, Phys. Rev. Lett. **55**, 1622 (1985).
- [17] B. N. Narozhny, I. L. Aleiner, Phys. Rev. Lett. **84**, 5383 (2000).
- [18] A. S. Price *et al.*, Science **316**, 99 (2007).
- [19] B. L. Altshuler, A. G. Aronov, Electron-electron interactions in disordered systems (North-Holland, Amsterdam, 1985).
- [20] J. Berezovsky, et al., Nanotechnology **21**, 274013 (2010).